Journal of Cleaner Production 264 (2020) 121720

Contents lists available at ScienceDirect

Journal of Cleaner Production

journal homepage: www.elsevier.com/locate/jclepro

Synthetic natural gas production from CO_2 and renewable H_2: Towards large-scale production of Ni–Fe alloy catalysts for commercialization

Huong Lan Huynh [a], Wakshum Mekonnen Tucho [b], Xinhai Yu [c], Zhixin Yu [a, *]

[a] Department of Energy and Petroleum Engineering, University of Stavanger, 4036, Stavanger, Norway
[b] Department of Mechanical and Structural Engineering and Material Science, University of Stavanger, 4036, Stavanger, Norway
[c] State Key Laboratory of Bioreactor Engineering, East China University of Science and Technology, 200237, Shanghai, China

ARTICLE INFO

Article history:
Received 18 January 2020
Received in revised form
9 March 2020
Accepted 13 April 2020
Available online 20 April 2020

Handling editor: Bin Chen

Keywords:
Power-to-Gas
CO_2 methanation
Ni–Fe alloy Catalyst
Hydrotalcite precursors
Space-time yield

ABSTRACT

Synthetic natural gas (SNG) is one of the promising energy carriers for the excessive electricity generated from variable renewable energy sources. SNG production from renewable H_2 and CO_2 via catalytic CO_2 methanation has gained much attention since CO_2 emissions could be simultaneously reduced. In this study, Ni–Fe/(Mg,Al)O_x alloy catalysts for CO_2 methanation were prepared via hydrotalcite precursors using a rapid coprecipitation method. The effect of total metal concentration on the physicochemical properties and catalytic behavior was investigated. Upon calcination, the catalysts showed high specific surface area of above 230 $m^2\ g^{-1}$. Small particle sizes of about 5 nm were obtained for all catalysts, even though the produced catalyst amount was increased by 10 times. The catalysts exhibited excellent space-time yield under very high gas space velocity (34,000 h^{-1}), irrespective of the metal concentration. The CO_2 conversions reached 73–79% at 300 °C and CH_4 selectivities were at 93–95%. Therefore, we demonstrated the potential of large-scale production of earth-abundant Ni–Fe based catalysts for CO_2 methanation and the Power-to-Gas technology.

© 2020 The Authors. Published by Elsevier Ltd. This is an open access article under the CC BY license (http://creativecommons.org/licenses/by/4.0/).

1. Introduction

Fossil fuels including coal, oil, and natural gas have been our primary energy sources to supply the rising needs of heating, cooling, lighting, transportation, and other energy demands. However, fossil fuels are not replenished, and its combustion releases a massive amount of greenhouse gas CO_2 into the atmosphere, which is partially responsible for global warming and climate change (Rashid et al., 2019, 2020). Hence, the development of a sustainable low-carbon economy is urgently needed for our future energy system (Song, 2006). In recent years, the shift towards renewable energy sources (RES), like wind and solar energy, has substantially occurred. In the European power sector, for instance, RES are expected to contribute half of the total gross electricity generation in 2030 (Agora Energiewende and Sandbag, 2019). Clean energy produced from RES is practically unlimited but highly dependent on weather conditions. Consequently, the mismatch between energy supply and demand necessitates the development of large-scale and flexible energy storage technologies for the transformation of surplus electricity.

Synthetic or substitute natural gas (SNG), an effective energy carrier with high heating value, is one of the promising chemical compounds for energy storage (Rönsch et al., 2016). With the existing infrastructure including pipeline networks, storage facilities, and filling stations, SNG can be distributed and stored without additional expenses. This is an advantage of using SNG as energy carrier compared to hydrogen, for instance. Traditionally, SNG is produced from coke oven gas, or syngas from coal or wood, or biomass (Kopyscinski et al., 2010). Since the 1970s, considerable efforts have been devoted to the application of CO and CO_2 methanation reactions for the production of SNG.

$$CO_2 + 4H_2 \leftrightarrow CH_4 + 2H_2O \quad (1)$$

CO_2 methanation (Eq. (1)), known as the Sabatier reaction, has gained renewed attention due to the emerging Power-to-Gas concept. On the one hand, this technology can converge the value chains of both gas and electricity sectors into one energy system,

* Corresponding author.
E-mail address: zhixin.yu@uis.no (Z. Yu).

https://doi.org/10.1016/j.jclepro.2020.121720
0959-6526/© 2020 The Authors. Published by Elsevier Ltd. This is an open access article under the CC BY license (http://creativecommons.org/licenses/by/4.0/).

Abbreviations

GHSV	Gas Hourly Space Velocity
HT	Hydrotalcite
LDH	Layered Double Hydroxides
RES	Renewable Energy Sources
RWGS	Reverse Water Gas Shift
SEM	Scanning Electron Microscopy
S_i	Product Selectivity
SMSI	Strong Metal-Support Interaction
SNG	Synthetic Natural Gas
STP	Standard Temperature and Pressure
STY	Space Time Yield
TEM	Transmission Electron Microscopy
TOS	Time On Stream
TPD	Temperature-Programmed Desorption
TPR	Temperature-Programmed Reduction
WHSV	Weight Hourly Space Velocity
X_{CO2}	CO_2 Conversion
XRD	X-Ray Diffraction

allowing flexible handling and storage of surplus renewable electricity. On the other hand, the process also tackles greenhouse gases emission by large-scale recycling of CO_2. Hydrogen (H_2) is produced via water electrolysis using renewable electricity, which further reacts with CO_2 (e.g., directly captured from the air) to form methane (CH_4). The produced SNG, also called renewable natural gas, can be used in natural gas end-use appliances, such as mobility and residential heating or being injected into the existing gas grid (Bailera et al., 2017).

Catalytic CO_2 methanation was discovered for more than a century by (Sabatier and Senderens, 1902). Although the reaction is thermodynamically favorable at low temperatures and elevated pressures, high activation energy is required to overcome the thermodynamic barrier of extremely stable CO_2 molecules (Vogt et al., 2019). Many different metals such as Ni, Co, Fe, Cu, Ru, Rh, Ir, Pd, and Pt have been exploited. Despite the fact that noble metals (i.e., Ru, Rh) are highly active and produce exclusively CH_4, Ni-based catalysts have always been the first choice for industrial catalysts due to its availability and affordable price (Aziz et al., 2015; Ghaib and Ben-Fares, 2018).

Rational design and synthesis of new catalytic materials play an important role in the enhancement of industrial process efficiency. Recently, by taking advantage of molecular simulations such as density functional theory, not only the kinetics of methanation reaction can be described but preliminary screening of new catalytic models can also be performed (Nørskov et al., 2009). According to the Pareto-optimal set, when both the catalytic activity and price of the catalysts were under consideration, nickel-iron (Ni_3Fe) alloys were found to be a promising candidate to substitute the noble-metal catalysts (e.g., Ru) with higher activity than each individual constituent in methanation (Andersson et al., 2006). Moreover, the Ni–Fe alloy catalysts are relatively cheaper than pure Ni catalysts. Many experimental studies have been carried out and confirmed the superiority of Ni–Fe alloy catalysts. It has also shown that the optimal compositions of Ni and Fe depend on the supports and metal loadings (Kustov et al., 2007). Ni–Fe alloys on Al_2O_3 were found to be less active than on $MgAl_2O_4$ for CO hydrogenation to CH_4 at 225 °C. Moreover, at a low metal loading of 2.5 wt%, the 75Ni25Fe alloy catalyst exhibited the highest conversion. Meanwhile, the 50Ni50Fe alloy catalyst performed better at a higher metal loading of 10 wt%. Different supports, namely Al_2O_3, ZrO_2, TiO_2, SiO_2, and Nb_2O_5 were investigated for CO_2 hydrogenation to CH_4 at 250 °C ($H_2/CO_2 = 24/1$). The Ni_3Fe alloy on Al_2O_3 support emerged as the best catalyst with the highest activity at total metal loading of both 10 wt% and 15 wt% (Pandey and Deo, 2016; Ray and Deo, 2017). In another study, unsupported Ni–Fe catalysts were also studied. It revealed that Ni–Fe alloy with Fe/Ni molar ratio of approximately 0.1 performed better than Ni_3Fe and monometallic catalysts (Pandey et al., 2018). Recently, it has been reported that the Fe/Ni molar ratio of 0.1 was the optimal composition of Ni–Fe/(Mg,Al)O_x catalysts for CO_2 methanation at 335 °C (Mebrahtu et al., 2018). It would be interesting to investigate the performance of Ni–Fe catalysts derived from HTs for CO_2 methanation over a wide temperature range for practical applications.

In the methanation unit of Power-to-Gas pilot plants, Ni-based catalysts are commonly used (Bailera et al., 2017). Besides the activity and selectivity, the main concern of Ni-based catalysts for industrial applications is catalyst deactivation, possibly due to metal sintering and/or carbon formation. CO_2 methanation is a highly exothermic reaction (Eq. (1), $\Delta H = -165.0$ kJ mol^{-1}). Thus, hotspots could possibly occur in the catalyst bed and cause thermal agglomeration of Ni active sites, which consequently reduced the catalysts' stability. To address these problems, it was recommended that well-defined crystalline structures like solid solution, spinel, perovskite, rigid mesoporous frameworks, or core-shell structures could be used to synthesize highly dispersed and stable Ni active sites. Reinforcing strong metal-support interaction (SMSI) was also suggested due to their ability to enhance not only the activity but also the stability of heterogeneous catalysts (Li et al., 2019). On the other hand, lowering CO_2 activation energy by enhanced chemisorption and dissociation of CO_2 could be achieved on the catalytic surfaces with strong basicity. The combination of alkaline oxides MgO and Al_2O_3 has been reported as the best catalytic support for CO_2 conversion reactions, due to its strong basicity and good thermal stability (Fan, M.-T. et al., 2014). Interestingly, the Lewis basic (Mg,Al)O_x mixed oxide can be derived from hydrotalcite-like materials (Bette et al., 2016).

Hydrotalcite (HT) materials, also called layered double hydroxides (LDH), have gained much attention for the synthesis of supported catalysts. The general formula for HT-like material is $[M^{2+}_{1-x}M^{3+}_x(OH)_2](A^{n-})_{x/n} \bullet mH_2O$, where M represents metals, and A is anion (Cavani et al., 1991). HT-like precursors offer access to well-dispersed and homogeneous metallic sites with SMSI after thermal decomposition and activation (i.e., calcination and reduction, respectively). Upon reduction, small and thermally stable metal nanoparticles were formed from the mixed metal oxides. Another compelling interest of this material is driven by its compositional flexibility with a wide choice of metal cations (Fan, G. et al., 2014). Conventionally, HT-like precursors are synthesized by coprecipitation method. The coprecipitation between the mixed salt solutions and the base solution was carried out by a slow addition rate (i.e., dropwise addition in several hours), leading to slow nucleation and simultaneous agglomeration (Othman et al., 2009). Recently, rapid coprecipitation for HT synthesis has been reported, where mixed salt solutions were quickly injected into a base solution within minutes (Tathod and Gazit, 2016). The nucleation rate was high with relatively slow crystal growth. Upon calcination, the obtained catalysts have small and uniform particle sizes as well as narrow pore size distribution, which are important features of catalysts prepared from HT precursors with rapid coprecipitation. This method was also considered as a highly efficient and facile procedure for HTs synthesis since it was fast and simple. Unfortunately, only small quantities of catalysts were produced from the original reported work, which focused on the fundamentals of nucleation and growth of HT crystals.

In this study, Ni–Fe/(Mg,Al)O_x HT-derived catalysts were prepared by rapid coprecipitation with Ni loading of 20 wt% and Fe loading of 2 wt%, corresponding to a Fe/Ni molar ratio of 0.1. The catalysts have been maintained at a Ni loading of 20 wt%, which is close to the loading of commercial Ni catalysts. The HT precursors with high purity and crystallinity were successfully synthesized in large quantities by rapid coprecipitation, which is more facile, energy-efficient and environmental-friendly compared to the conventional method. The catalysts were tested in CO_2 methanation in the temperature range of 200–450 °C and at a high space velocity of 34,000 h^{-1}. All Ni–Fe catalysts showed excellent activity, selectivity and high stability in CO_2 methanation. Moreover, we confirmed that large-scale production of HT-derived catalysts for the commercial application of CO_2 methanation was possible without interfering with the catalytic activity and stability. To the best of our knowledge, this is the first study to explore the upscale potential of Ni–Fe alloy catalysts via rapid coprecipitation for CO_2 methanation at industrial relevant conditions.

2. Experimental

2.1. Catalyst preparation

All reagents were analytical grade (Merck Millipore) and used as received without purification. The procedure was adapted from (Tathod and Gazit, 2016). In a typical preparation, mixed salt solutions consisting of $Ni(NO_3)_2.6H_2O$, $Fe(NO_3)_3.9H_2O$, $Mg(NO_3)_2.6H_2O$ and $Al(NO_3)_3.9H_2O$ with total metal concentration of 0.25M, 1M and 2.5M were used. 100 mL of the mixed salt solution was rapidly injected by a syringe into a 500 mL base solution containing a sufficient amount of NaOH and Na_2CO_3 under vigorous stirring at 60 °C. The suspension was then aged under flowing N_2 at 85 °C for 18 h. Subsequently, the gel-like mass was filtered, washed until the pH of the filtrate was neutral, and dried at 90 °C overnight. The dried precursors were calcined at 600 °C for 6 h in flowing synthetic air (heating rate of 5 K min^{-1}). In all catalysts, the Ni and Fe loading were kept constant at 20 wt% and 2 wt%, respectively, which corresponding to a Fe/Ni molar ratio of 0.1. The ratio between divalent and trivalent cations was fixed at 3. The catalysts were denoted as NiFe-*x*M, where *x* is the total metal concentration used during preparation.

The calcined samples were reduced and passivated for further characterization. The calcined catalysts were reduced at 600 °C for 4 h (heating rate of 5 K min^{-1}) under 50 vol% H_2/N_2 with a total flow of 100 mL min^{-1} (STP). Upon reduction, the samples were cooled down to room temperature in flowing N_2 (total flow of 50 mL min^{-1}, STP). Thereafter, synthetic air was added to adjust the oxygen content in the gas mixture to 0.1 vol% and then 1 vol% to passivate the catalysts.

2.2. Catalyst characterization

X-ray diffraction (XRD) patterns were recorded on a Bruker D8 Advance micro-diffractometer using CuKα radiation source in the 2θ range of 5-90° at a step interval of 1° min^{-1}. The *d*-spacing was calculated based on Bragg's law (Cullity, 1956). The average crystallite size *d* was calculated by the Scherrer equation (Eq. (2) (Cullity, 1956),), where K_F is the shape factor (0.9), λ is the wavelength of CuKα (1.5406 Å), θ is the diffraction angle of the peak and β represents the full width at half maximum of the peak (in radians).

$$d = \frac{K_F \times \lambda}{\beta \times cos\theta} \quad (2)$$

The N_2 adsorption-desorption isotherms were determined at −196 °C using Micromeritics Tristar 3000 instrument. Prior to measurement, the sample (~120 mg) was degassed overnight at 150 °C under vacuum. The surface area was calculated by the BET method in the pressure range of $0.05 < P/P_o < 0.3$. The pore volume and pore size distribution were calculated from the desorption branch of the isotherms by the BJH method.

Temperature programmed reduction (TPR) of the calcined catalysts and temperature-programmed desorption (TPD) of the reduced catalysts were carried out by Micromeritics Autochem II ASAP 2020 instrument equipped with a thermal conductivity detector (TCD). The calcined sample (~100 mg) was first degassed at 200 °C for 30 min and then reduced using 10 vol% H_2/Ar from 50 °C to 950 °C at a heating rate of 10 K min^{-1}. Subsequently, TPD measurement was conducted on the reduced sample by degassing at 600 °C in He for 30 min. A flow of 6 vol% CO_2/Ar was then introduced for 1 h. Weakly adsorbed CO_2 was desorbed by He flow for 1 h. The CO_2-TPD was recorded by heating up the sample to 800 °C under He flow at a heating rate of 10 K min^{-1}. The same equipment was also used to measure TPR data of reduced catalysts in order to determine the reduction degree (Eq. (3)) (Marocco et al., 2018).

$$Reduction\ degree\ f\ (\%) = \frac{TPR\ peak\ area\ of\ calcined\ sample - TPR\ peak\ area\ of\ reduced\ sample}{TPR\ peak\ area\ of\ calcined\ sample} \times 100 \quad (3)$$

H_2 chemisorption analysis was performed at 35 °C on Micromeritics ASAP 2020 Plus instrument. Calcined samples (~200 mg) were degassed in He flow at 200 °C for 2 h, reduced in H_2 flow at 600 °C for 4 h (heating rate of 5 K min^{-1}), and cooled down to 35 °C prior to measurement. The chemisorption of H_2 was assumed to occur only on Ni atom with an adsorption stoichiometry of one hydrogen atom per nickel atom. The dispersion of Ni active sites was calculated by Eq. (4) (Bartholomew, 1975), where n_{H2} is the mol of H_2 uptake in chemisorption study, w_{Ni} is weight percentage, *f* is the reduction degree and M_{Ni} is the molar mass of Ni.

$$Ni\ dispersion\ (\%) = \frac{number\ of\ Ni\ at\ surface}{total\ number\ of\ Ni} = \frac{2 \times n_{H2} \times M_{Ni}}{w_{Ni} \times f/100} \times 100 \quad (4)$$

The morphology of the precursors was examined using Gemini Supra 35VP (ZEISS) Scanning Electron Microscopy (SEM). The dried powder samples were spread on carbon tape and coated with Pd plasma to inhibit charging. Further analyses were performed using JEM-2100F (JEOL) Transmission Electron Microscopy (TEM) working at 200 kV. The reduced-passivated powder samples were dissolved in ethanol, assisted by ultrasonic dispersion. A drop of the suspension was deposited on a holey carbon-coated copper grid.

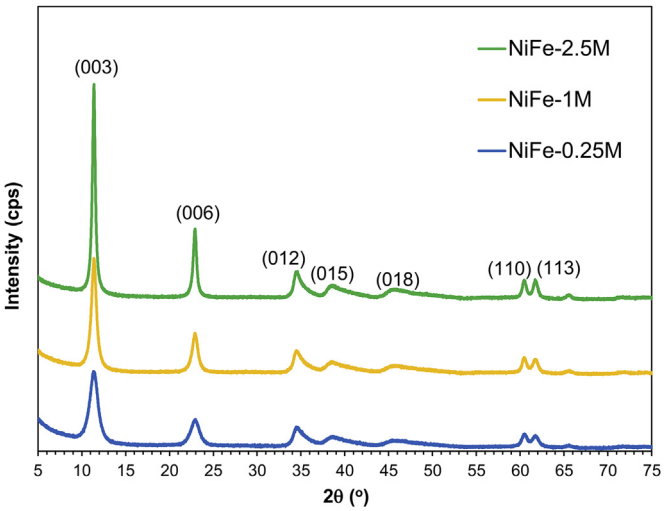

Fig. 1. XRD patterns of HT precursors.

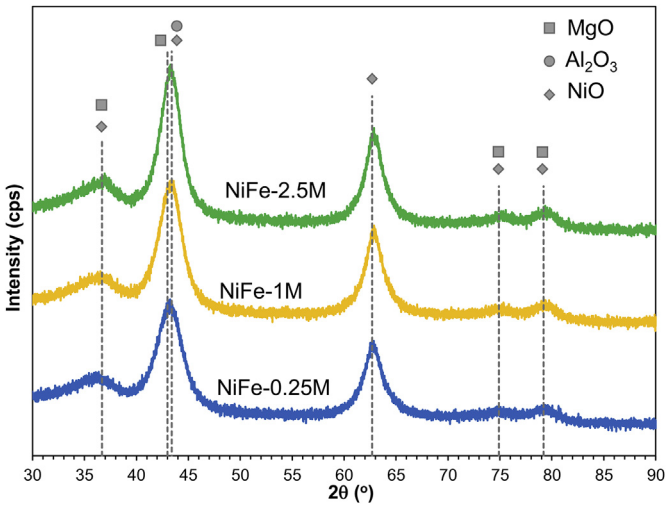

Fig. 2. XRD patterns of calcined catalysts.

2.3. Activity tests

CO_2 methanation was conducted in a stainless steel fixed-bed reactor (inner diameter of 4.5 mm) heated by an electric oven at atmospheric pressure. The temperature was controlled by a K-type thermocouple installed in the bottom of the catalyst bed. The flow rate of reactant gases was regulated by calibrated mass flow controllers (Alicat). In a typical experiment, 60 mg of calcined catalysts (pressed and sieved into particles of 300–355 μm) was diluted with 600 mg of silicon carbide (SiC, grit 45, particle size of 355 μm) and placed on the quartz wool, located above the thermocouple. Prior to reaction, the catalyst was reduced at 600 °C for 4 h in 50 vol% H_2/N_2 with a total flow of 100 mL min^{-1} (STP). Thereafter, the reactor was cooled down in pure N_2 flow for 1 h. Residual H_2 from reduction was purged out from the reactor. Subsequently, the reactant gases of $H_2/N_2/CO_2$ in a ratio of 64/20/16 (i.e., $H_2/CO_2 = 4/1$) was introduced at 270 mL min^{-1} (STP), corresponding to a weight hourly space velocity (WHSV) of 270 L g_{cat}^{-1} h^{-1} or a gas hourly space velocity (GHSV) of 34,000 h^{-1} with regards to the catalytic bed length of 3 cm. The CO_2 methanation tests were run at 200–450 °C at ambient pressure and were maintained at steady state for 1 h at each temperature. Water formed during the reaction was condensed by a cold trap operating at 1 °C. The outgases were analyzed using an online gas chromatograph (Agilent 7890A). A blank test was conducted, and no significant conversion was found over SiC powder in the stainless steel reactor.

The CO_2 conversion (X_{CO2}), CH_4 and CO selectivity (S_i) and space-time yield (STY) of CH_4 were defined in Eqs. (5)–(7), where F^{in} and F^{out} are the molar flow rates (mol h^{-1}), V^{in} is the volumetric flow rates (cm^3 h^{-1}) and V_R is the volume of the catalytic bed (cm^3).

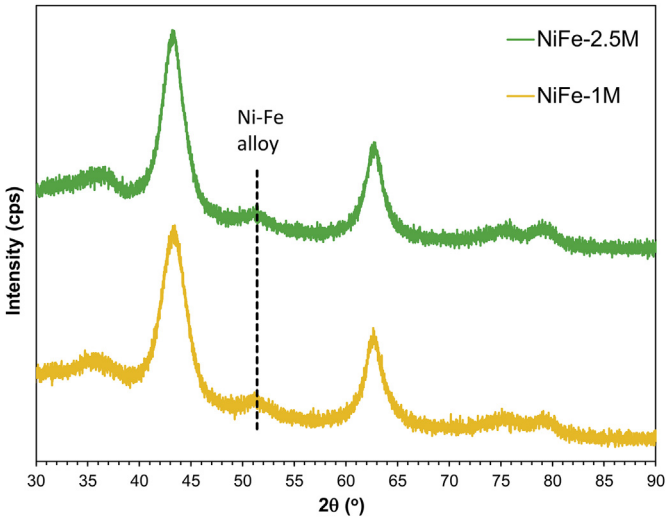

Fig. 3. XRD patterns of reduced-passivated catalysts.

$$X_{CO2}\ (\%) = \frac{F_{CO2}^{in} - F_{CO2}^{out}}{F_{CO2}^{in}} \times 100 \quad (5)$$

$$S_i(\%) = \frac{F_i^{out}}{F_{CO2}^{in} - F_{CO2}^{out}} \times 100 \quad (6)$$

Table 1
Physicochemical properties of as-prepared HT precursors.

Precursors	Lattice cell parameter *a* (Å) *	Lattice cell parameter *c* (Å) *	Crystallite size (nm)	Mass obtained per batch (g)	BET surface area (m^2 g^{-1})	BJH pore volume (cm^3 g^{-1})
NiFe-0.25M	3.06	23.31	7.9	1.90	218.8	0.45
NiFe-1M	3.06	23.29	12.8	7.66	158.8	0.46
NiFe-2.5M	3.06	23.29	22.0	18.77	114.4	0.30
Reference (Delidovich and Palkovits, 2015)	3.07	23.81	5.8	–	118	0.40

*$a = 2 \times d(110)$ and $c = 3 \times d(003)$.

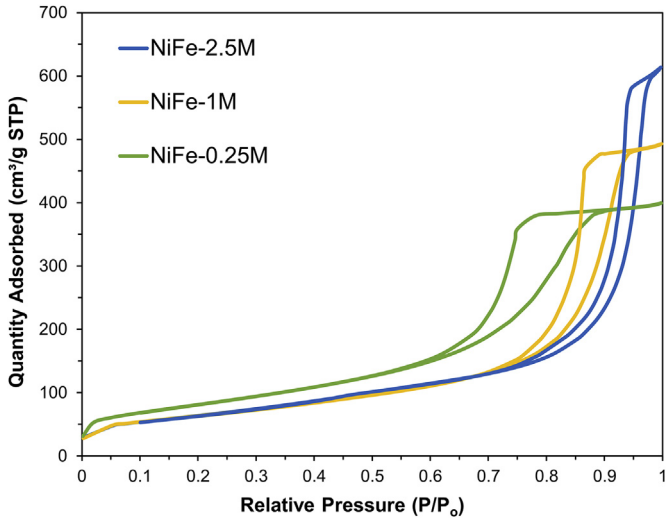

Fig. 4. N_2 physisorption isotherms of calcined catalysts.

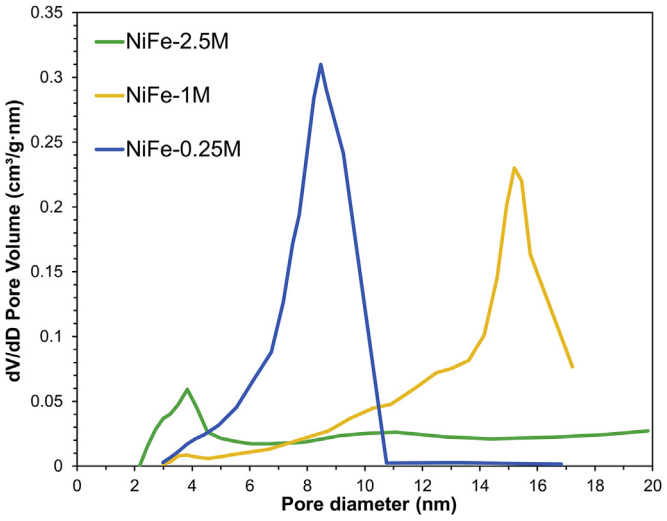

Fig. 5. BJH pore size distribution of calcined catalysts.

$$STY_{CH4}(h^{-1}) = \frac{X_{CO2} \times S_{CH4} \times V_{CO2}^{in}}{1000 \times V_R} \quad (7)$$

The stability tests were conducted at 350 °C for 12 h and at 300 °C for 65 h using the same procedure and condition.

3. Results and discussion

3.1. Catalysts characterization

The presence of hydrotalcite in the as-prepared precursors was confirmed by XRD analysis (Fig. 1). The XRD patterns of the precursors show common features of LDH structures (MgAl-HT JCPDS 01-089-0460) with symmetric and sharp reflections of the basal (003), (006), (012) planes at 2θ of 11.4°, 22.9°, and 34.5°, respectively. Broader and smaller peaks at 2θ of 38.5°, 45.6°, 60.5°, and 61.8° could be ascribed to the nonbasal (015), (018), (110) and (113) planes, respectively. No other phases were identifiable in the XRD diffractograms. Thus, it can be inferred that HT precursors with high purity and crystallinity were successfully synthesized by rapid coprecipitation, regardless of metal concentrations.

It was reported that HT materials have layered structures in rhombohedral 3R symmetry and the parameters of a unit cell, *a* and *c*, could be derived from *d* (110) and *d* (003) spacing (Cavani et al., 1991). The thickness of one layer consisting of a brucite-like sheet and one interlayer could be estimated based on the *d*-spacing of the (003) plane. Meanwhile, the average cation-cation distance in the brucite-like layer could be correlated to the *d*-spacing of the (110) plane. The lattice parameters of as-prepared precursors are summarized in Table 1. Interestingly, there was no significant difference

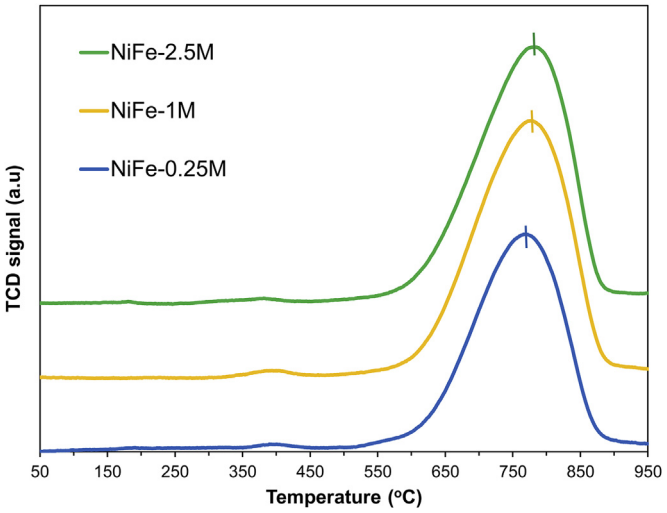

Fig. 6. H_2-TPR profiles of calcined catalysts.

in the lattice parameters between precursors prepared at different concentrations. Moreover, the unit cells of all precursors were slightly smaller than that of the reference material, $Mg_{0.75}Al_{0.25}CO_3(OH)_{0.125}\bullet\ 0.71H_2O$ (Delidovich and Palkovits, 2015). This could be due to the substitution of smaller Ni^{2+} ion for larger Mg^{2+} ion (i.e., radii of 0.69 Å and 0.72 Å, respectively) in the layered structures. Thus, Ni (and Fe) cations were assumed to incorporate well into the HT structures. The crystallite size of the precursors was calculated from the (003) reflection using Scherrer's

Table 2
Physicochemical properties of calcined catalysts.

Catalysts	Oxide crystallite size (nm)	BET surface area (m^2 g^{-1})	BJH pore volume (cm^3 g^{-1})	Ni surface area (m^2 g^{-1})	Reduction degree	Ni Dispersion	Ni–Fe crystallite size (nm)
NiFe-0.25M	4.6	294.7	0.68	3.38	66%	4.07%	–
NiFe-1M	4.9	240.6	0.77	3.91	69%	4.48%	4.8
NiFe-2.5M	5.1	231.4	0.45	4.00	68%	4.68%	5.1

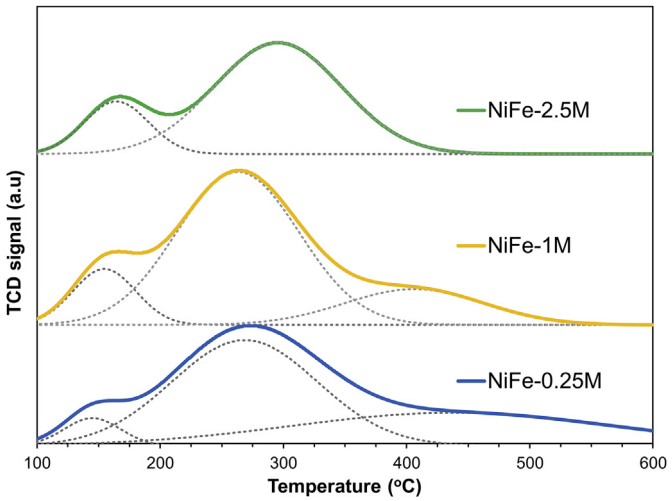

Fig. 7. CO_2-TPD profiles of reduced catalysts.

equation (Table 1). The crystallite size was larger than that of the reference material. As the metal concentration increased, larger crystals were obtained. Furthermore, it can be seen that a significantly larger amount of catalyst mass was obtained by increasing the total metal concentration during coprecipitation (Table 1).

Upon calcination, the HT structures were completely decomposed since only diffraction patterns of oxide phases were detected (Fig. 2). It was reported that only the rock-salt-type phase (NiO or MgO) was observed when Ni–Mg–Al HT precursors were calcined at a moderate calcination temperature of 600 °C. When the calcination temperature increased to 800 °C and above, the crystalline spinel phase such as $MgAl_2O_4$ was detected (Mette et al., 2014). In this study, the main reflection peaks could be attributed to not only NiO (JCPDS 01-089-5881) but also MgO (JCPDS 03-065-0476) and Al_2O_3 (JCPDS 01-073-1512). However, it is difficult to distinguish these phases due to overlapped diffraction patterns.

The XRD patterns of reduced-passivated catalysts are shown in Fig. 3. The formation of Ni–Fe alloy was confirmed by the representative peak of Ni_3Fe (200) at 2θ of 51.2° (JCPDS 03-065-3244). Diffraction peaks of MgO and Al_2O_3 were still apparent in the

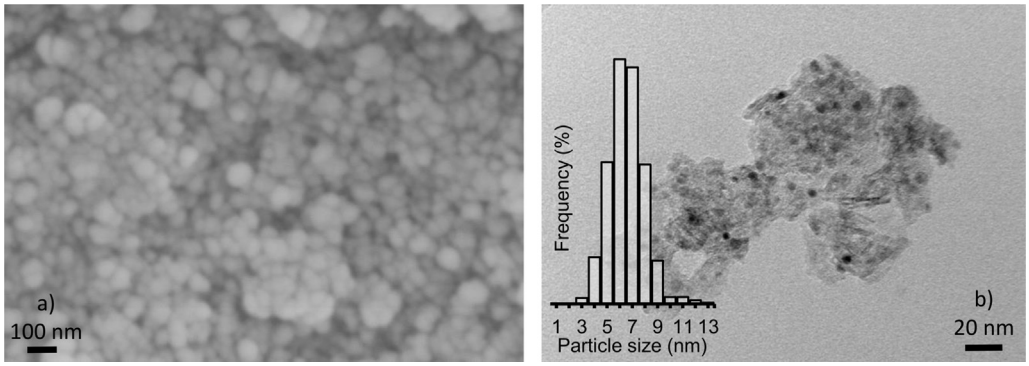

Fig. 8. a) SEM images of NiFe-1M HT precursors; b) TEM bright-field images of reduced-passivated NiFe-1M catalyst. The inset in (b) is the particle size distribution.

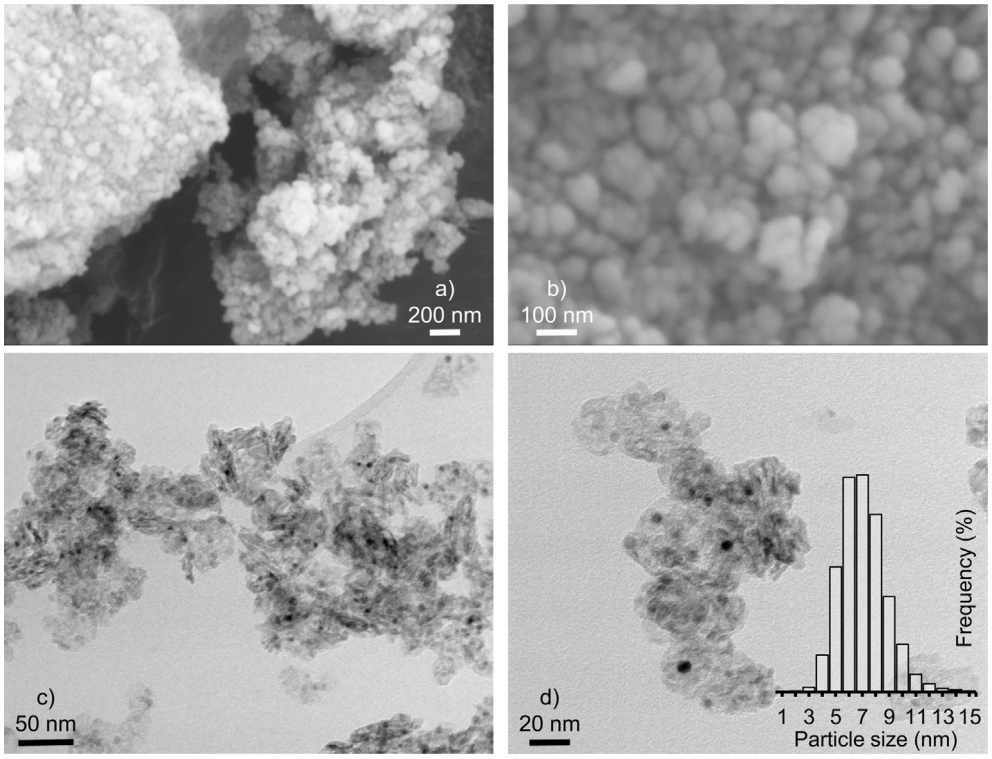

Fig. 9. a-b) SEM images of NiFe-2.5M HT precursors; c-d) TEM bright-field images of reduced-passivated NiFe-2.5M catalyst. The inset in (d) is the particle size distribution.

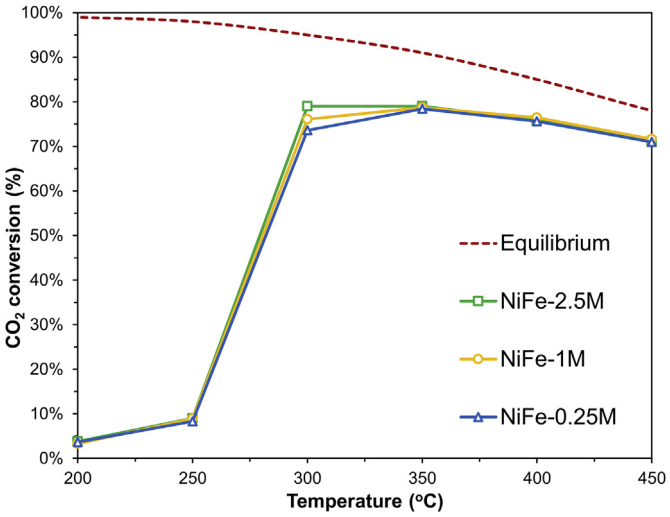

Fig. 10. CO_2 conversion *vs* temperature of different Ni–Fe/(Mg,Al)O_x catalysts in CO_2 methanation; the dashed line is the thermodynamic equilibrium.

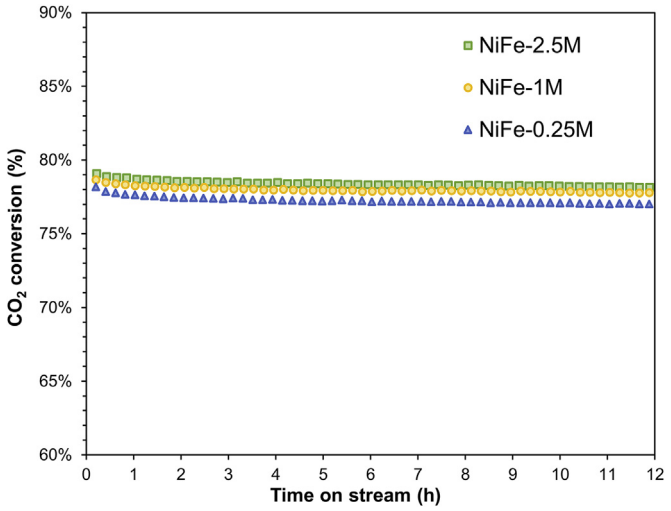

Fig. 12. CO_2 conversion of different Ni–Fe/(Mg,Al)O_x catalysts in CO_2 methanation at 350 °C.

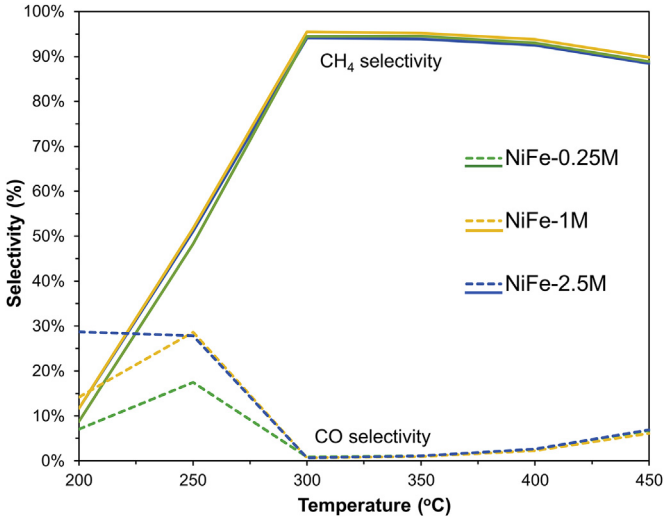

Fig. 11. CH_4 and CO selectivity *vs* temperature of different Ni–Fe/(Mg,Al)O_x catalysts in CO_2 methanation.

reduced-passivated samples. The calculated crystallite size of Ni–Fe alloy was close to the oxide crystallite size of the calcined catalysts of ca. 5 nm (Table 2), which are further independent of the total metal concentration during preparation.

The textural properties of calcined catalysts are summarized in Table 2. The N_2 adsorption-desorption isotherms show a type IV isotherm with hysteresis at high P/P_o range, which is characteristic of mesoporous materials (Fig. 4). Compared to the textural properties of as-prepared precursors (Table 1), the calcined catalysts had higher surface area and pore volume. Upon calcination at 600 °C, the layered structures collapsed, resulting in higher surface area and larger pore channels. However, with increasing metal concentration, the surface area and pore volume decreased. Nevertheless, all calcined catalysts exhibited a high surface area (230–300 $m^2\ g^{-1}$) and pore volume (0.4–0.8 $cm^3\ g^{-1}$) compared to conventional catalysts (Mebrahtu et al., 2018). Catalysts prepared by the rapid coprecipitation method also possessed a uniform pore structure according to their pore size distribution (Fig. 5). The pore size of the calcined NiFe-0.25M catalyst was 8–10 nm, while the pore size of the calcined NiFe-1M catalyst was larger at 14–16 nm. Interestingly, the structure of the calcined NiFe-2.5M catalyst consisted of significantly small pores of ~4 nm. It is worth mentioning that this tunable pore dimension by different metal concentrations in this study can be employed in other reactions such as Fischer-Tropsch synthesis (Khodakov et al., 2002).

To study the reducibility of different catalysts, TPR analysis was conducted. All H_2-TPR profiles exhibit one intense peak at a high temperature range of 760–800 °C (Fig. 6), ascribed to the reduction of NiO species to metallic Ni. This is to be compared with the reduction peak of pure NiO at 290–340 °C (Beierlein et al., 2019). The reduction of iron oxide species was negligible by small peaks at ~400 °C due to low Fe content in the catalysts. A fine distribution of NiO was assumed, resulting in stronger interaction and thus a higher reduction temperature (Guo et al., 2004; Rostrup-Nielsen, 1984). For catalysts prepared at higher metal concentrations, the reduction peaks slightly shifted to higher temperatures. However, it can be assumed that the reducibility of all three catalysts was similar, regardless of the total metal concentration during preparation.

CO_2-TPD has been carried out to study the surface basicity. The desorption profiles (Fig. 7) show three peaks corresponding to weak, medium and strong basic sites (Di Cosimo et al., 1998). The NiFe-1M catalyst possessed the highest total basicity among the others since its integrated area under the desorption line was the largest, which is expected to perform better catalytic activity. However, the impact of different basic types (weak, medium, and strong) on the catalytic activity in CO_2 methanation remains ambiguous. The strong basic site was suggested to be the dominant factor by (He et al., 2014) while (Aldana et al., 2013) convinced that the weak basic site was more responsible for the improvement of catalytic activity.

The Ni surface area was calculated from the adsorbed amount of H_2 based on the chemisorption study. H_2 was assumed to adsorb only on Ni atoms and not Fe atoms. For the determination of metal dispersion, the reduction degree was calculated (Table 2), reconfirmed the similar reducibility of all catalysts. Moreover, as the metal concentration increased, the Ni–Fe alloy catalysts exhibited slightly higher Ni surface area and better Ni dispersion.

The SEM characterization revealed an agglomerated morphology of NiFe-1M (Fig. 8a) and NiFe-2.5M HT precursors (Fig. 9ab). Spherical agglomerates were observed for both

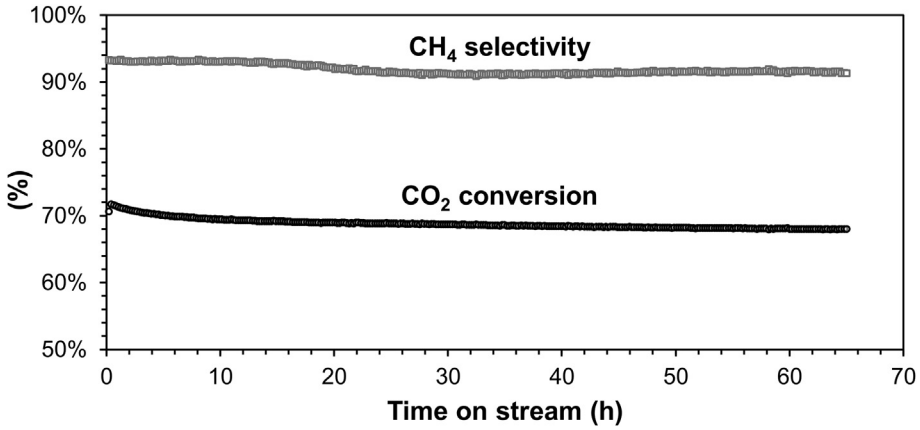

Fig. 13. CO_2 conversion and CH_4 selectivity during a long-term test of NiFe-1M catalyst in CO_2 methanation at 300 °C.

Table 3
Specific methane production rate of our catalysts and different catalytic systems for CO_2 methanation ($H_2/CO_2 = 4$) reported in the literature.

Catalysts	Ni wt%	Preparation method	T (°C)	Space velocity of CO_2	Specific CH_4 productivity ($mol_{CH4}\ g_{Ni}^{-1}\ h^{-1}$)	STY (h^{-1})
Ni–Fe/(Mg,Al)O_x HT	20	Coprecipitation	300	5440 h^{-1} or 43.2 $L.g_{cat}^{-1}.h^{-1}$	7.01	3954
(NiFe-1M)			350		7.22	4076
Ni–Fe/(Mg,Al)O_x HT Mebrahtu et al. (2018)	12	Coprecipitation	335	2115 h^{-1}	0.47	–
Ni(Al)O_x HT [a] Abelló et al. (2013)	69.1	Coprecipitation	400	44.8 $L.g_{cat}^{-1}.h^{-1}$	2.65	–
Ni/(Mg,Al)O_x HT Liu et al. (2016)	17.2	Coprecipitation	300	360 h^{-1}	0.02	332
Ni/Al_2O_3 [b] (Bengaouer et al., 2018)	14–17	Commercial catalyst	250	526 h^{-1}	0.187	437
Ni/Al_2O_3 HT (Abate et al., 2016)	76	Coprecipitation	300	750 h^{-1}	–	487.5
Ni/ZrO_2 (Jia et al., 2019)	8.68	Impregnation	300	9600 h^{-1}	1.27	2845
Ni/TiO_2 (Zhou et al., 2016)	10	Impregnation	350	12,000 h^{-1}	6.39	3600
Ni/La_2O_3 (Song et al., 2010)	10	Impregnation	350	5100 h^{-1}	1.88	4131
Ni–Ce/USY zeolite (Graça et al., 2014)	14	Impregnation	400	7036 h^{-1}	2.92	4570
Ni/CeO_2–ZrO_2 (Aldana et al., 2013)	5	Pseudo sol-gel	350	7052 h^{-1}	2.55	5581

[a] Reaction at 10 bar.
[b] Reaction at 4 bar, the desirable temperature was 250 °C but the actual temperature inside the reactor was 400–540 °C.

precursors. TEM images of the reduced-passivated catalysts show the highly dispersed Ni–Fe round-shaped particles (dark color) on the support (Figs. 8b and 9cd). The average particle size from the TEM images was obtained by measuring about 750–800 particles for each sample using ImageJ software. Notably, the increase in total metal concentration did not significantly affect the average size of Ni–Fe alloy particles, which was approximately 6.0 ± 1.4 nm for NiFe-1M and 6.5 ± 1.7 nm for the NiFe-2.5M catalyst. These results are also close to the crystallite size obtained from the XRD study.

3.2. Catalytic activity

The activity of Ni–Fe/(Mg,Al)O_x catalysts for CO_2 methanation was studied in the temperature range of 200–450 °C at a stoichiometric H_2/CO_2 ratio of 4. A high GHSV of 34,000 h^{-1} was used. Although CO_2 methanation was thermodynamically favored at low temperatures, kinetic limitation prevents the reaction to readily occur. As expected, poor performance at 200–250 °C is observed for all catalysts (Fig. 10). From 250 °C to 300 °C, CO_2 conversions plunged up from approximately 10% to 73–79%. The conversions slightly declined at 350–450 °C because of the thermodynamics of methanation reaction (Gao et al., 2012).

The CH_4 selectivity reached 93–95% at 300–450 °C for all catalysts (Fig. 11). The production of CH_4 was not significant at low temperatures of 200–250 °C. Meanwhile, a small amount of CO was also formed, probably from the reverse water gas shift reaction (RWGS, $CO_2 + H_2 \leftrightarrow CO + H_2O$). The selectivity of CO increased at 400–450 °C because CO production via RWGS was thermodynamically favored at high temperatures. Overall, the activity of all three catalysts were not significantly different. By increasing the total metal concentration during preparation (up to 10 times higher), a larger amount of catalyst mass was obtained but their catalytic performance remained unchanged. This demonstrates the feasibility of large-scale preparation of catalysts by our proposed method in this study.

The stability of all catalysts at a fixed temperature of 350 °C is presented in Fig. 12. All catalysts exhibited satisfactory stability and good performance during 12 h time on stream (TOS) despite slight deactivation. CO_2 conversions of ca. 78% are in line with the result of the temperature-dependent activity tests (Fig. 10). A long-term test of NiFe-1M catalysts was also carried out at 300 °C (Fig. 13). The initial CO_2 conversion was 71.78% and reduced to 68.09% after 65 h TOS, corresponding to a deactivation rate of only 0.057% h^{-1} (Mutz et al., 2017). reported a deactivation rate of 0.12% h^{-1} of 20 wt% Ni/Al_2O_3 commercial catalysts in CO_2 methanation at 358 °C, 6 bar, and WHSV of 80.5 $L_{CO2}\ g_{cat}\ h^{-1}$. Under the same condition but at 305 °C, the prepared 17 wt% Ni_3Fe/Al_2O_3 catalysts showed a deactivation of 0.3% h^{-1}. Thus, our Ni–Fe/(Mg,Al)O_x can be assumed to have better stability than the commercial and other alumina supported catalysts.

The specific productivity of methane ($mol_{CH4}\ g_{Ni}^{-1}\ h^{-1}$) and

space-time yield (STY, the number of molecules produced per unit volume of reactor per unit time) of different catalysts in CO_2 methanation tested at high space velocity of CO_2 are summarized in Table 3. Overall, our Ni−Fe/(Mg,Al)O_x catalysts showed the highest specific methane productivity compared to the commercial catalyst, Ni/Al_2O_3 HT catalyst and other catalytic systems in literature. Although our space-time yield was slightly lower than La- and Ce-promoted catalysts, the price and availability of Ni−Fe/(Mg,Al)O_x catalyst is more attractive for the development of commercial catalysts for CO_2 methanation (U.S. Geological Survey, 2019).

4. Conclusions

Ni−Fe/(Mg,Al)O_x HT-derived catalysts were successfully prepared by rapid coprecipitation. The method was reproducible, energy-efficient and environmental-friendly for supported catalysts preparation compared to conventional synthesis. Overall, the prepared catalysts exhibited almost similar physicochemical properties, such as reducibility and particle sizes. Moreover, insignificant differences in catalytic performance were obtained for all Ni−Fe/(Mg,Al)O_x catalysts in CO_2 methanation. Thus, by increasing the total metal concentration, larger amount of catalyst mass per batch was obtained while the catalytic activity was maintained. It revealed a great opportunity for a mass production of highly active Ni−Fe/(Mg,Al)O_x HT-derived catalysts. The scaled-up catalysts performed significantly high conversion of CO_2 (up to 79%) and CH_4 selectivity (up to 95%) at 300 °C under relevant industrial conditions (high GHSV of 34,000 h^{-1}, $H_2/CO_2 = 4$). The specific rate of methane production and space-time yield was higher than many reported catalytic systems in literature. Ni−Fe/(Mg,Al)O_x HT-derived catalysts with outstanding performance and high potential for large-scale production emerge as a promising candidate for the commercialization of CO_2 methanation process to produce SNG from renewable H_2 and CO_2.

Declaration of competing interest

The authors declare that they have no known competing financial interests or personal relationships that could have appeared to influence the work reported in this paper.

CRediT authorship contribution statement

Huong Lan Huynh: Investigation, Validation, Writing - original draft, Visualization. **Wakshum Mekonnen Tucho:** Investigation, Resources, Writing - review & editing. **Xinhai Yu:** Resources, Supervision. **Zhixin Yu:** Methodology, Writing - review & editing, Supervision, Project administration.

Acknowledgments

The authors would like to thank the Norwegian Ministry of Education and Research and Valide AS through the Plogen Program for financial support.

References

Abate, S., Barbera, K., Giglio, E., Deorsola, F., Bensaid, S., Perathoner, S., Pirone, R., Centi, G., 2016. Synthesis, characterization, and activity pattern of Ni−Al hydrotalcite catalysts in CO2 methanation. Ind. Eng. Chem. Res. 55 (30), 8299−8308.

Abelló, S., Bolshak, E., Montané, D., 2013. Ni−Fe catalysts derived from hydrotalcite-like precursors for hydrogen production by ethanol steam reforming. Appl. Catal., A 450, 261−274.

Aldana, P.A.U., Ocampo, F., Kobl, K., Louis, B., Thibault-Starzyk, F., Daturi, M., Bazin, P., Thomas, S., Roger, A.C., 2013. Catalytic CO2 valorization into CH4 on Ni-based ceria-zirconia. Reaction mechanism by operando IR spectroscopy. Catal. Today 215, 201−207.

Andersson, M.P., Bligaard, T., Kustov, A., Larsen, K.E., Greeley, J., Johannessen, T., Christensen, C.H., Nørskov, J.K., 2006. Toward computational screening in heterogeneous catalysis: Pareto-optimal methanation catalysts. J. Catal. 239 (2), 501−506.

Aziz, M.A.A., Jalil, A.A., Triwahyono, S., Ahmad, A., 2015. CO2 methanation over heterogeneous catalysts: recent progress and future prospects. Green Chem. 17 (5), 2647−2663.

Bailera, M., Lisbona, P., Romeo, L.M., Espatolero, S., 2017. Power to Gas projects review: Lab, pilot and demo plants for storing renewable energy and CO2. Renew. Sustain. Energy Rev. 69, 292−312.

Bartholomew, C.H., 1975. Alloy catalysts with monolith supports for methanation of coal-derived gases. Quarterly Progress Report to ERDA.

Beierlein, D., Häussermann, D., Pfeifer, M., Schwarz, T., Stöwe, K., Traa, Y., Klemm, E., 2019. Is the CO2 methanation on highly loaded Ni-Al2O3 catalysts really structure-sensitive? Appl. Catal., B 247, 200−219.

Bengaouer, A., Ducamp, J., Champon, I., Try, R., 2018. Performance evaluation of fixed-bed, millistructured, and metallic foam reactor channels for CO2 methanation. Can. J. Chem. Eng. 96 (9), 1937−1945.

Bette, N., Thielemann, J., Schreiner, M., Mertens, F., 2016. Methanation of CO2 over a (Mg,Al)Ox supported nickel catalyst derived from a (Ni,Mg,Al)-Hydrotalcite-like precursor. ChemCatChem 8 (18), 2903−2906.

Cavani, F., Trifirò, F., Vaccari, A., 1991. Hydrotalcite-type anionic clays: preparation, properties and applications. Catal. Today 11 (2), 173−301.

Cullity, B.D., 1956. Elements of X-Ray Diffraction. Addison-Wesley Pub. Co.

Delidovich, I., Palkovits, R., 2015. Structure−performance correlations of Mg−Al hydrotalcite catalysts for the isomerization of glucose into fructose. J. Catal. 327, 1−9.

Di Cosimo, J.I., Dıez, V.K., Xu, M., Iglesia, E., Apesteguıa, C.R., 1998. Structure and surface and catalytic properties of Mg-Al basic oxides. J. Catal. 178 (2), 499−510.

Fan, G., Li, F., Evans, D.G., Duan, X., 2014a. Catalytic applications of layered double hydroxides: recent advances and perspectives. Chem. Soc. Rev. 43 (20), 7040−7066.

Fan, M.-T., Miao, K.-P., Lin, J.-D., Zhang, H.-B., Liao, D.-W., 2014b. Mg-Al oxide supported Ni catalysts with enhanced stability for efficient synthetic natural gas from syngas. Appl. Surf. Sci. 307, 682−688.

Gao, J., Wang, Y., Ping, Y., Hu, D., Xu, G., Gu, F., Su, F., 2012. A thermodynamic analysis of methanation reactions of carbon oxides for the production of synthetic natural gas. RSC Adv. 2 (6), 2358−2368.

Ghaib, K., Ben-Fares, F.-Z., 2018. Power-to-Methane: a state-of-the-art review. Renew. Sustain. Energy Rev. 81, 433−446.

Graça, I., González, L.V., Bacariza, M.C., Fernandes, A., Henriques, C., Lopes, J.M., Ribeiro, M.F., 2014. CO2 hydrogenation into CH4 on NiHNaUSY zeolites. Appl. Catal., B 147, 101−110.

Guo, J., Lou, H., Zhao, H., Chai, D., Zheng, X., 2004. Dry reforming of methane over nickel catalysts supported on magnesium aluminate spinels. Appl. Catal., A 273 (1), 75−82.

He, L., Lin, Q., Liu, Y., Huang, Y., 2014. Unique catalysis of Ni-Al hydrotalcite derived catalyst in CO2 methanation: cooperative effect between Ni nanoparticles and a basic support. J Energy Chem 23 (5), 587−592.

Jia, X., Zhang, X., Rui, N., Hu, X., Liu, C.-j., 2019. Structural effect of Ni/ZrO2 catalyst on CO2 methanation with enhanced activity. Appl. Catal., B 244, 159−169.

Khodakov, A.Y., Griboval-Constant, A., Bechara, R., Zholobenko, V.L., 2002. Pore size effects in fischer tropsch synthesis over cobalt-supported mesoporous silicas. J. Catal. 206 (2), 230−241.

Kopyscinski, J., Schildhauer, T.J., Biollaz, S.M.A., 2010. Production of synthetic natural gas (SNG) from coal and dry biomass − a technology review from 1950 to 2009. Fuel 89 (8), 1763−1783.

Kustov, A.L., Frey, A.M., Larsen, K.E., Johannessen, T., Nørskov, J.K., Christensen, C.H., 2007. CO methanation over supported bimetallic Ni−Fe catalysts: from computational studies towards catalyst optimization. Appl. Catal., A 320, 98−104.

Li, J., Lin, Y., Pan, X., Miao, D., Ding, D., Cui, Y., Dong, J., Bao, X., 2019. Enhanced CO2 methanation activity of Ni/Anatase catalyst by tuning strong metal−support interactions. ACS Catal. 9 (7), 6342−6348.

Liu, J., Bing, W., Xue, X., Wang, F., Wang, B., He, S., Zhang, Y., Wei, M., 2016. Alkaline-assisted Ni nanocatalysts with largely enhanced low-temperature activity toward CO2 methanation. Catal. Sci. Technol. 6 (11), 3976−3983.

Marocco, P., Alexandru Morosanu, E., Giglio, E., Ferrero, D., Asmelash, C., Lanzini, A., Abate, S., Bensaid, S., Perathoner, S., Santarelli, M., Pirone, R., Centi, G., 2018. CO2 methanation over Ni/Al hydrotalcite-derived catalyst: experimental characterization and kinetic study. Fuel 225, 230−242.

Mebrahtu, C., Krebs, F., Perathoner, S., Abate, S., Centi, G., Palkovits, R., 2018. Hydrotalcite based Ni−Fe/(Mg, Al)Ox catalysts for CO2 methanation − tailoring Fe content for improved CO dissociation, basicity, and particle size. Catal. Sci. Technol. 8 (4), 1016−1027.

Mette, K., Kühl, S., Düdder, H., Kähler, K., Tarasov, A., Muhler, M., Behrens, M., 2014. Stable performance of Ni catalysts in the dry reforming of methane at high temperatures for the efficient conversion of CO2 into syngas. ChemCatChem 6 (1), 100−104.

Mutz, B., Belimov, M., Wang, W., Sprenger, P., Serrer, M.-A., Wang, D., Pfeifer, P., Kleist, W., Grunwaldt, J.-D., 2017. Potential of an alumina-supported Ni3Fe catalyst in the methanation of CO2: impact of alloy formation on activity and stability. ACS Catal. 7 (10), 6802−6814.

Nørskov, J.K., Bligaard, T., Rossmeisl, J., Christensen, C.H., 2009. Towards the

computational design of solid catalysts. Nat. Chem. 1, 37.
Othman, M.R., Helwani, Z., Martunus, Fernando, W.J.N., 2009. Synthetic hydrotalcites from different routes and their application as catalysts and gas adsorbents: a review. Appl. Organomet. Chem. 23 (9), 335–346.
Pandey, D., Deo, G., 2016. Determining the best composition of a Ni–Fe/Al2O3 catalyst used for the CO2 hydrogenation reaction by applying response surface methodology. Chem. Eng. Commun. 203 (3), 372–380.
Pandey, D., Ray, K., Bhardwaj, R., Bojja, S., Chary, K.V.R., Deo, G., 2018. Promotion of unsupported nickel catalyst using iron for CO2 methanation. Int. J. Hydrogen Energy 43 (10), 4987–5000.
Rashid, K., Ellingwood, K., Safdarnejad, S.M., Powell, K.M., 2019. Designing flexibility into a hybrid solar thermal power plant by real-time, adaptive heat integration. In: Muñoz, S.G., Laird, C.D., Realff, M.J. (Eds.), Computer Aided Chemical Engineering. Elsevier, pp. 457–462.
Rashid, K., Mohammadi, K., Powell, K., 2020. Dynamic simulation and techno-economic analysis of a concentrated solar power (CSP) plant hybridized with both thermal energy storage and natural gas. J. Clean. Prod. 248, 119193.
Ray, K., Deo, G., 2017. A potential descriptor for the CO2 hydrogenation to CH4 over Al2O3 supported Ni and Ni-based alloy catalysts. Appl. Catal., B 218, 525–537.
Rönsch, S., Schneider, J., Matthischke, S., Schlüter, M., Götz, M., Lefebvre, J., Prabhakaran, P., Bajohr, S., 2016. Review on methanation – from fundamentals to current projects. Fuel 166, 276–296.
Rostrup-Nielsen, J.R., 1984. Catalytic steam reforming. In: Anderson, J.R., Boudart, Michel (Eds.), Catalysis. Springer, p. 1.
Sabatier, P., Senderens, J.-B., 1902. Nouvelles syntheses du methane. Comptes Rendus Des Séances De L'Académie Des Sciences, Section VI – Chimie 134, 514–516.
Song, C., 2006. Global challenges and strategies for control, conversion and utilization of CO2 for sustainable development involving energy, catalysis, adsorption and chemical processing. Catal. Today 115 (1), 2–32.
Song, H., Yang, J., Zhao, J., Chou, L., 2010. Methanation of carbon dioxide over a highly dispersed Ni/La2O3 catalyst. Chin. J. Catal. 31 (1), 21–23.
Tathod, A.P., Gazit, O.M., 2016. Fundamental insights into the nucleation and growth of Mg–Al layered double hydroxides nanoparticles at low temperature. Cryst. Growth Des. 16 (12), 6709–6713.
U.S. Geological Survey, 2019. Mineral commodity summaries 2019. U.S. Geological Survey. https://doi.org/10.3133/70202434.
Vogt, C., Monai, M., Kramer, G.J., Weckhuysen, B.M., 2019. The renaissance of the Sabatier reaction and its applications on Earth and in space. Nat. Catal. 2 (3), 188–197.
Zhou, R., Rui, N., Fan, Z., Liu, C.-j., 2016. Effect of the structure of Ni/TiO2 catalyst on CO2 methanation. Int. J. Hydrogen Energy 41 (47), 22017–22025.
Agora Energiewende and Sandbag (2019): The European Power Sector in 2018. Up-to-date analysis on the electricity transition.